

Supporting Information

Undercoordinated Active Sites on 4H Gold Nanostructures for CO₂ Reduction

Yuxuan Wang,^{1,†} Chenyang Li,^{2,†} Zhanxi Fan,^{4,5} Ye Chen,⁶ Xing Li,³ Liang Cao,² Canhui Wang,¹ Lei Wang,¹ Dong Su,³ Hua Zhang,^{4,5} Tim Mueller,^{2,*} and Chao Wang^{1,*}

¹Department of Chemical and Biomolecular Engineering and ²Department of Materials Science and Engineering, Johns Hopkins University, Baltimore, Maryland 21218, United States

³Center for Functional Nanomaterials, Brookhaven National Laboratory, Upton, New York 11973, United States

⁴Department of Chemistry, City University of Hong Kong, Kowloon, Hong Kong, China

⁵Hong Kong Branch of National Precious Metals Material Engineering Research Center (NPMM), City University of Hong Kong, Hong Kong, China

⁶Center for Programmable Materials, School of Materials Science and Engineering, Nanyang Technological University, Singapore, 639798, Singapore

*Email: chaowang@jhu.edu; tmueller@jhu.edu.

[†]Equal contribution.

Experimental Methods

Materials. Hydrogen tetrachloroaurate (III) hydrate ($\text{HAuCl}_4 \cdot x\text{H}_2\text{O}$, ~49% Au basis), lead (II) nitrate ($\text{Pb}(\text{NO}_3)_2$, 99.999%) were purchased from Alfa Aesar. Oleylamine (70%, technical grade), Borane tert-butylamine complex (BTB, 97%), sodium hydroxide (NaOH, semiconductor grade, 99.99%), potassium bicarbonate (KHCO_3 , $\geq 99.95\%$) were purchased from Sigma Aldrich. All the materials were used without further purification. Electrolyte solutions were prepared using 18.2 M Ω H_2O (Elga Veolia).

Synthesis of 4H-Au Nanoribbons. In a typical experiment, HAuCl_4 (4.08 mg) and oleylamine (220 μl) were dissolved in hexane (3.54 ml) and 1,2-dichloropropane (250 μl). The mixture in a closed glass vial was then heated in a water bath at 58 °C for 16 h. After that, the resulting product was collected using centrifugation (5,000 r.p.m., 1 min), washed at least three times with hexane and then re-dispersed into hexane (4 ml).

Synthesis of 4H- and fcc-Au Nanorods. 4H Au nanorods was synthesized following methods published by Zhang, et al., with slight modification.¹⁻² $\text{HAuCl}_4 \cdot x\text{H}_2\text{O}$ (30 mg) was added to oleylamine (4.8 ml) and sonicated until fully dissolved. The solution was left undisturbed at 70 °C in a furnace for 25 hours and subsequently centrifuged with hexane and ethanol (9:1 ratio) four times to purify and precipitate the nanorods. The final product was redispersed in hexane. To convert Au nanorods from the 4H to fcc phase, the 4H Au nanorods were heated at 185 °C in a furnace overnight. The resulting Au nanorods only exhibits fcc crystal structure.

Sample Characterizations. Transmission Electron Microscopy (TEM) images were acquired on a FEI Tecnai 12 microscope operated at 100 kV. Atomic resolution high angle annular dark field (HAADF) scanning transmission electron microscopy (STEM) images and elemental maps were

acquired with HD2700C STEM (Hitachi) equipped with a probe aberration corrector and Enfina spectrometer (Gatan). The X-ray diffraction patterns were obtained on X-ray powder diffraction (XRPD) data was collected on a laboratory Bruker D8 Focus diffractometer (40 kV, 40 mA, sealed Cu X-ray tube, $K\alpha_1$ 1.540596 Å, $K\alpha_2$ 1.544493 Å) with a Ni filter and LynxEye position sensitive detector at room temperature. The scattering range was $2\theta = 5\sim 120^\circ$ with a step size of 0.02° over 4 h set using DIFFRAC plus XRD Commander software. Inductively Coupled plasma mass spectrometry (ICP-MS) was performed on PerkinElmer NexION 300D with ICP.

Electrochemical Reduction of CO₂. The electrocatalytic properties of the Au electrocatalysts were measured using a custom-made gas-tight electrolysis cell and Autolab 302 potentiostat (Metrohm). A Hg/HgSO₄ electrode (Hach) and a Pt mesh (VWR) were used as the reference and counter electrode, respectively. A solution of 0.1 M KHCO₃ was used as electrolyte. CO₂ was bubbled through a glass frit to the cathode compartment at a constant rate of 20 sccm and purged for 10 minutes prior to each measurement. Working electrodes were prepared by spraying 40 µg (estimated) of Au nanorods and Au nanoparticles (dispersed in hexane) onto a carbon paper electrode (3.53 cm²). The actual weight of catalysts deposited was determined by ICP-AES after each test. The cathode and anode compartments were separated with an AHO anion exchange membrane (Selemion Inc.), which avoids or minimizes the possible transfer of chemical species (e.g., Pt dissolved from the counter electrode, products produced from the cathode) across the cell. The reference electrode was Hg/HgSO₄. All potentials in this work are converted to the reversible hydrogen electrode (RHE) scale by $E \text{ (vs RHE)} = E \text{ (vs Hg/HgSO}_4\text{)} + 0.64 \text{ V} + 0.0591 \times \text{pH}$, where the pH for 0.1 M KHCO₃ electrolyte saturated by CO₂ is 6.8. The gas-phase products were measured online using gas chromatograph-mass spectrometry (GC-MS) and liquid-phase products

were analyzed after 30 min of reaction at each potential using nuclear magnetic resonance (NMR) spectroscopy. The typical CO₂RR experiment takes around 3 hours.

Pb Under-potential Deposition. Relative populations of surface facets were probed using Pb under-potential deposition (UPD). Each electrode was swept between 0.05 V and 0.9 V in 0.1 M NaOH for 50 times to clean the surface prior to the measurement. Then they were cycled between 0.3 V and 0.7 in 0.1 M NaOH and 0.1 mM Pb (NO₃)₂ at 50 mV/s for five times, where the second scan was taken for analysis.

Cu Under-potential Deposition. The electrochemical surface areas of Au electrodes were measured via Cu under-potential deposition (Cu_{upd}). Each electrode was swept between 0.05 V and 0.9 V in 0.5 M H₂SO₄ for 50 times to clean the surface prior to the measurement. The electrodes were then cycled from 0.1 V to −0.3 V (vs. Hg/HgSO₄) at 50 mV/s. in 0.5 M H₂SO₄ solution containing 0.1 M CuSO₄. The electrolyte was purged with Ar continuously. The anodic stripping peak centered at −0.1 V was integrated using 92.4 μC/cm² as the conversion factor.³ The obtained surface areas were then used to normalize current densities and Pb_{upd} voltammetric profile.

Computational Methods

Cluster Expansion. Cluster expansions are generalized Ising models,⁴⁻⁵ in which the spin variables for each site in an Ising model are replaced by “site” variables that represent the species occupied at each site. A property (such as energy) of the material can be expressed as a linear expansion of cluster functions,

$$E(\mathbf{s}) = V_0 + \sum_{cluster} V_{cluster} \prod_{i \in cluster} s_i \quad (1)$$

where the coefficients V_0 and $V_{cluster}$ are effective cluster interactions (ECI) to be fitted to a set of DFT training data, and \mathbf{s} is the set of site variables. If all possible cluster functions are included in the cluster expansion, the above equation is exact. However, the ECIs for clusters that contain a large number of sites or the sites that are far apart are usually negligible. Thus, the cluster expansion can be truncated to a sum over finite numbers of cluster functions with little loss of accuracy.

To investigate the surface structures of Au nanorods, binary cluster expansions for fcc Au nanorod and 4H Au nanorod were generated based on the fcc and 4H lattice, where each site can be occupied by either a gold atom or a vacancy. For the nanorods in this paper, we represent the vacuum around the nanorods as a collection of sites that are occupied by vacancies, allowing us to use a training set of small (1~2 nm in diameter) nanorods to construct a cluster expansion that can be used to rapidly predict the energies of larger nanorods with varying shapes and sizes. The cluster expansions were truncated to include the empty cluster, the single-site cluster, all two-body clusters within a cutoff distance of 10 Å, all three-body clusters within a cutoff distance of 6 Å, and all four-body clusters within a cutoff distance of 3 Å, for a total of 28 and 110 symmetrically distinct cluster functions for the fcc and 4H Au cluster expansion, respectively. The nearest

neighbor distance for Au is 2.86 Å. Training sets with 51 and 77 relaxed structures (fcc and 4H nanorods) by density functional theory (DFT)⁶ calculations were generated and refined for fitting ECIs of the cluster expansions. The ECIs for these cluster functions were fit to the training sets using a Bayesian approach.⁷ This approach allows for more distinct ECIs to be included in the cluster expansion than there are structures in the training set, and this generally improves the predictive accuracy of the cluster expansion.⁷⁻⁹ The inverse of the covariance matrix for the prior was diagonal, with elements given by:

$$\lambda_{\alpha\alpha} = \begin{cases} 0, & n_{\alpha} = 0 \\ \lambda_1, & n_{\alpha} = 1 \\ \lambda_2 e^{\lambda_3 r_{\alpha}} e^{\lambda_4 n_{\alpha}}, & n_{\alpha} > 1 \end{cases} \quad (2)$$

where n_{α} is the number of sites in cluster function α , r_{α} is the maximum distance between sites, and λ_1 , λ_2 , λ_3 , and λ_4 were determined using a conjugate-gradient algorithm to minimize the leave-one-out cross-validation (LOOCV) error, which is a measurement of the prediction error.¹⁰ The resulting cluster expansions for fcc and 4H Au nanorods have LOOCV errors of 1.5 and 1.9 meV per atom, respectively.

DFT. DFT calculations have been performed using the Vienna Ab initio Simulation Package (VASP)¹¹ with the revised Perdew-Burke-Ernzerhof (RPBE)¹²⁻¹³ and PBEsol¹⁴ exchange-correlation functional. Van der Waals interactions were accounted for by using the D3 correction,¹⁵ and the VASPsol¹⁶ implicit solvation model was used to treat the effect of aqueous solution on adsorption energies. The Au_GW, C_GW, O_GW and H_GW PBE projector-augmented wave (PAW)¹⁷ potentials were used, and all VASP calculations were run with accurate precision, ensuring that there were no wrap-around errors. The Brillouin zone was sampled using efficient

grids generated by the k -point grid server¹⁸ with a minimum distance of 45.0 Å between adjacent points in real space lattice. Spin polarization was taken into account in the calculations and second-order Methfessel-Paxon smearing¹⁹ with a width of 0.2 eV was used to set partial occupancies. Real space projectors were used to evaluate the non-local part of the PAW potential. The convergence criteria for the electronic self-consistent iteration and the ionic relaxation loop were set to be 10^{-4} eV and 10^{-3} eV per cell, respectively. For Au nanorod cluster expansions and surface energy calculations, the PBEsol functional was used, as it is found to improve the equilibrium properties of solids and surfaces.²⁰ The convergence for surface energies and adsorption energies are 1 meV/Å² and 10 meV, respectively. The slabs are at least six layers thick, and the vacuum layers are at least 18 Å. Our calculation shows that RPBE-D3 gives overbinding to CO compared to experimentally measured CO adsorption energy on Au(211), whereas RPBE has a closer agreement with experiments.²¹⁻²² However, it is found that RPBE-D3 gives closer agreements on the onset potentials (related to *COOH binding energies) with experiments from this and previous study.²² Thus, we used RPBE energies for *CO and RPBE-D3 energies for *COOH in the free energy diagram. The hydrogen adsorption energies were calculated using the RPBE exchange-correlation functional.

Monte Carlo Simulation. Simulated annealing was used to find the ground-state shapes of the fcc and 4H Au nanorods. For each system studied, Monte Carlo simulations²³ were run from a high temperature (2000 K), and then decreased in steps by a factor of 4^{0.05} until room temperature. At each temperature, the number of Monte Carlo iterations was 50 times the number of sites in the supercell. Subsequent annealing was carried out by only allowing atoms to swap on the surface of the nanorods. The number of iterations was set to be 100 times the number of sites in the supercell. The supercells were 6 nm long (in the growing direction) and 7 nm wide (the nanorods

were 5 nm in diameter). The thermodynamically averaged properties, e.g. average fractions of different types of surface Pb sites, were recorded during the Monte Carlo sampling at room temperature (300 K).

Table S1. Comparison of J_{CO} and FE_{CO} reported in this work with the recent literature.

Samples	Electrolyte	Potential (V vs. RHE)	J_{CO} (mA/cm ² _{geo})	FE_{CO} (%)	Ref.
4H-Au nanoribbon	0.1 M KHCO ₃	−0.7	7.7	90	This work
8nm Au NPs	0.5 M KHCO ₃	−0.67	ca. 18	90	24
Au ₃ Cu NPs	0.1 M KHCO ₃	−0.9	ca. 3.4	67	25
rhombic dodecahedrons Au NPs	0.5 M KHCO ₃	−0.57	-	80	26
Au/carbon nanotubes	0.5 M NaHCO ₃	−0.5	-	94	27
Ag NPs	0.5 M KHCO ₃	−0.75	0.8	80	28
Mesostructured Ag	0.1 M KHCO ₃	−0.7	ca. 2.9	80	29

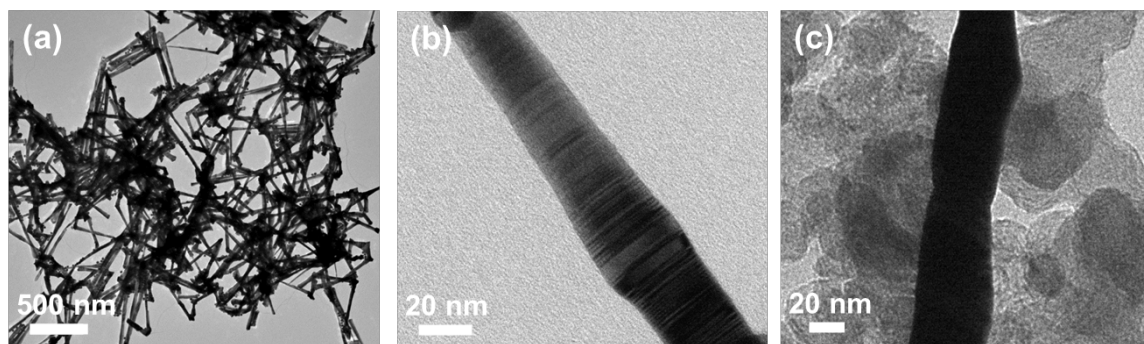


Figure S1. TEM images of (a, b) 4H/fcc-Au nanorods and (c) fcc-Au nanorods. These images indicate the Au nanorods have similar dimensions as compared to 4H-Au nanoribbons and fcc-Au nanorods maintain the nanorod morphology after thermal treatment.

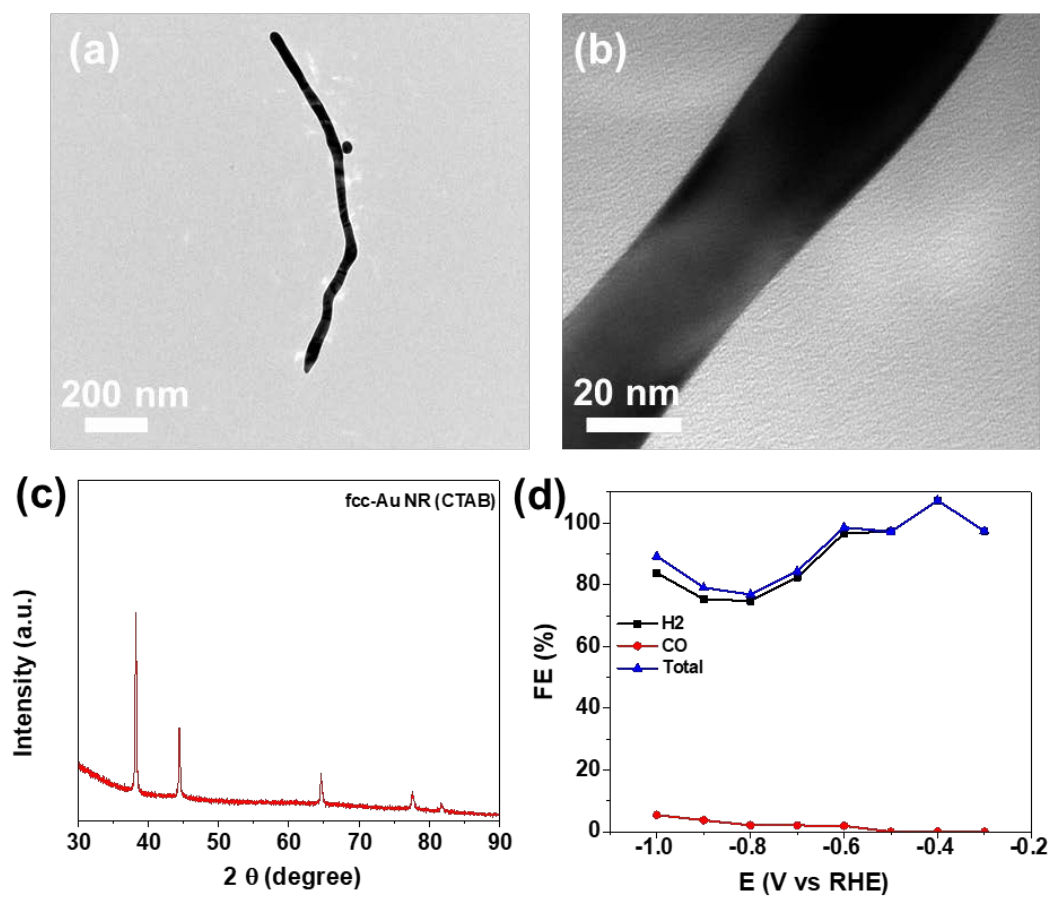


Figure S2. (a, b) TEM images for fcc Au nanorod with CTAB as binder and the corresponding (c) XRD patterns and (d) Faradaic efficiencies. This type of Au nanorod is thought to be poisoned by CTAB, thus having nearly no activity for CO₂ reduction.

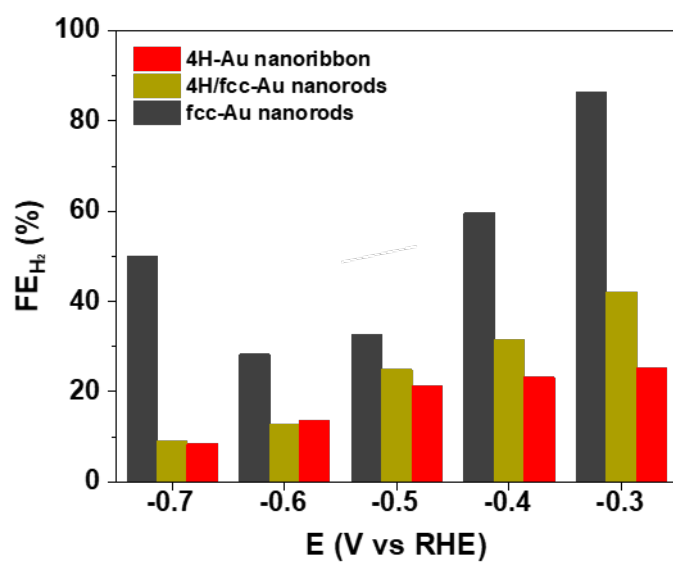


Figure S3. Faradaic Efficiency of H₂.

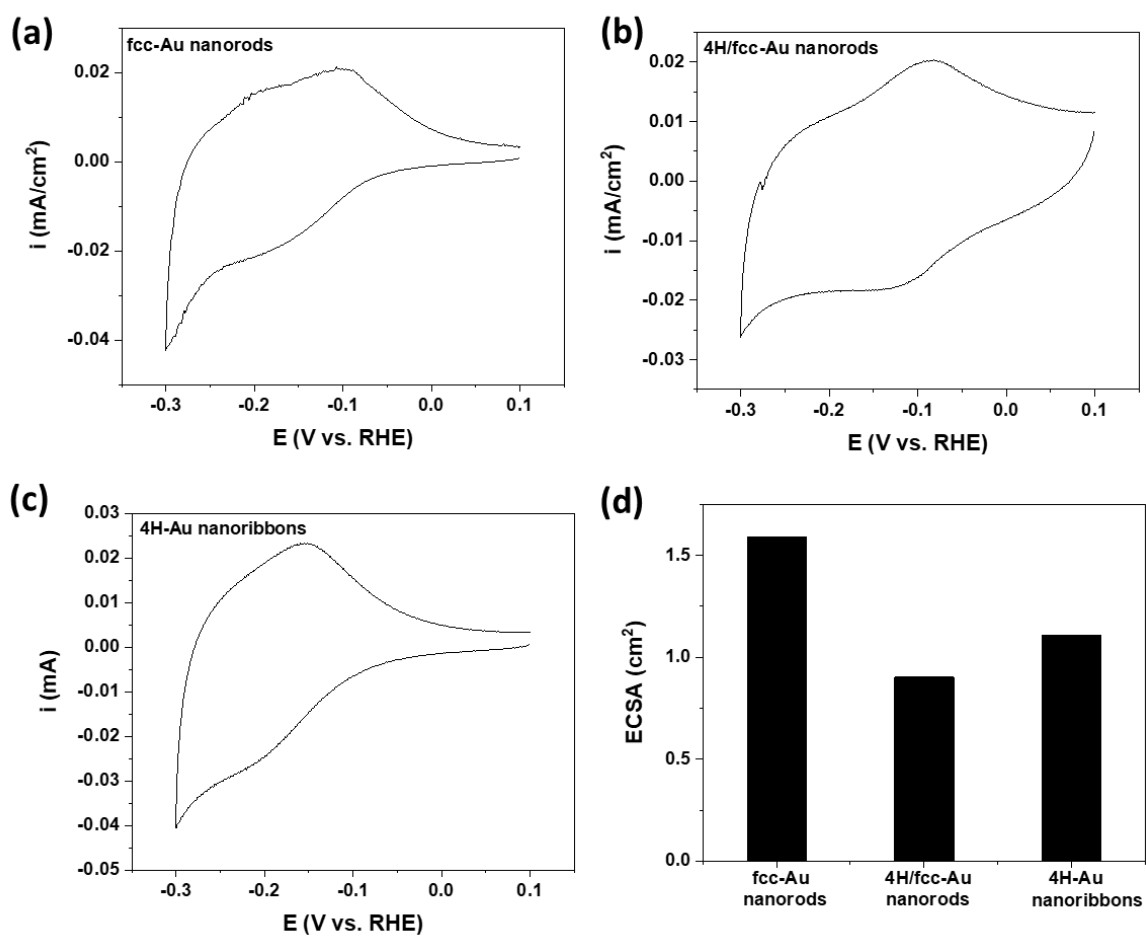


Figure S4. Cu_{upd} profiles and the calculated specific electrochemical active surface areas.

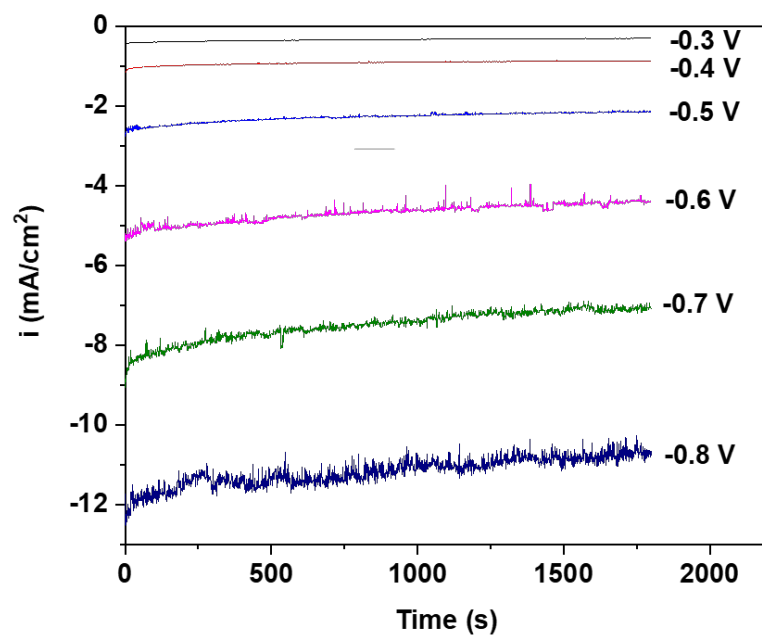


Figure S5. Typical current profile for 4H/fcc-Au nanorods in CO₂ reduction reaction.

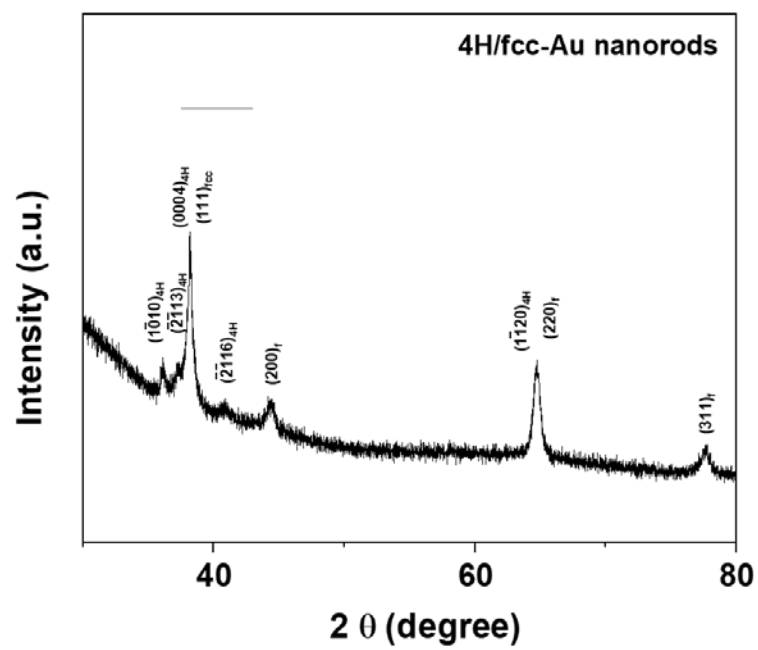


Figure S6. XRD pattern of 4H/fcc-Au nanorods after CO₂ reduction test.

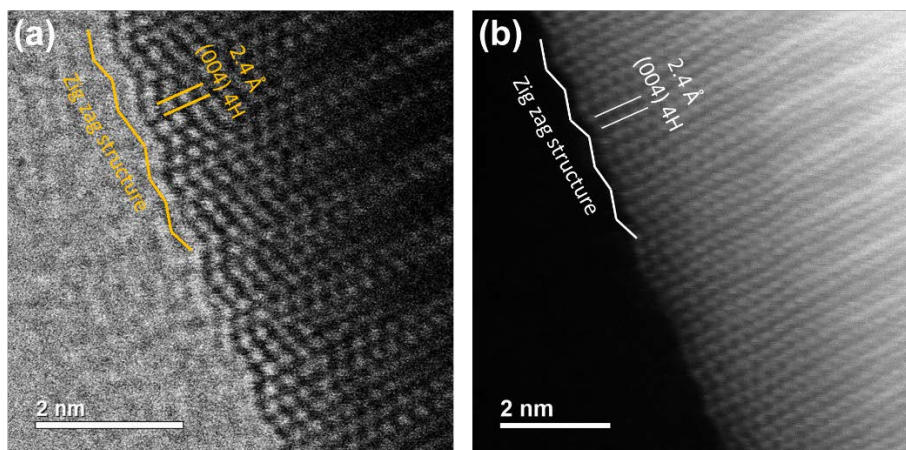


Figure S7. BF-STEM image (similar to TEM contrast) and HAADF image of 4H-Au nanoribbons after electrolysis test. Both image shows the 4H phase is well preserved during the test.

Table S2. DFT-calculated surface energies in this work. The “rec” denotes a reconstructed surface.

	Surface energy (eV/Å ²)
(100)	0.0724
(110)	0.0760
(110)-rec	0.0714
(111)	0.0607
(211)	0.0702
(311)	0.0740
(311)-rec	0.0731
(322)	0.0651
(332)	0.0640
4H(11 $\bar{1}$ 00)	0.0618
4H(11 $\bar{2}$ 0)	0.0759

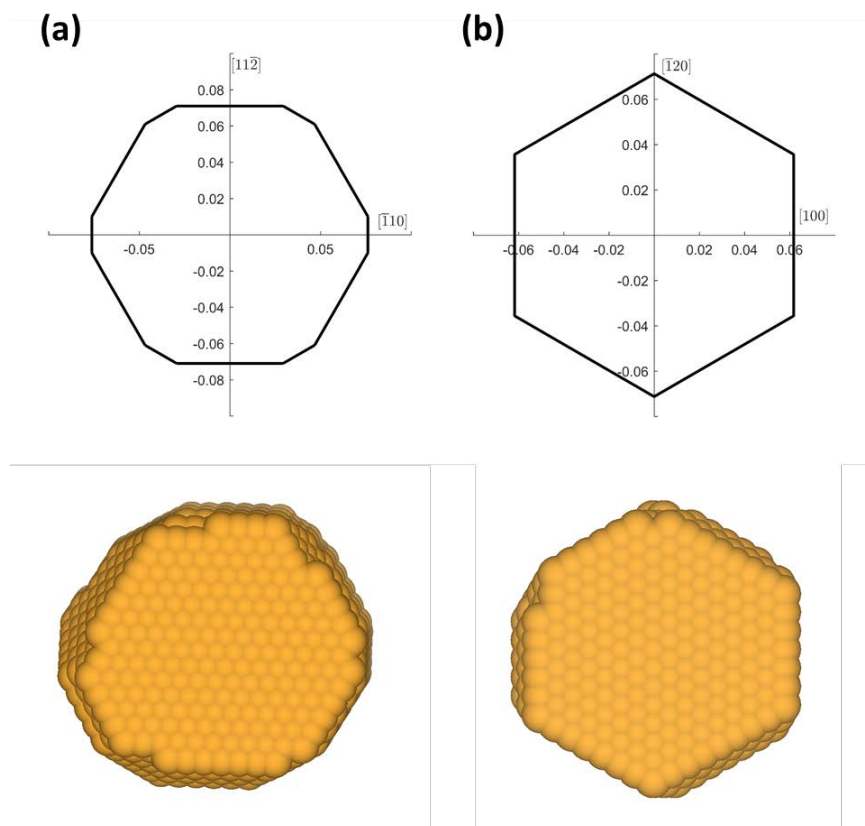


Figure S8. (Top) Wulff construction of (a) fcc, (b) 4H Au nanorod determined by DFT-calculated surface energies. (Bottom) Cluster-expansion-predicted equilibrium shapes of ~ 4 nm fcc and 4H nanorods.

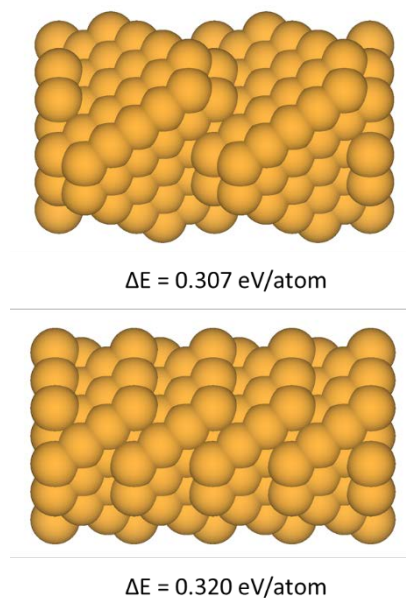


Figure S9. Two possible fcc-Au nanorod structures with 177 atoms per unit cell. (top) A cluster-expansion-predicted structure with (111) terraces. (bottom) A manually created structure having the same number of atoms per simulation cell but more (211) steps. DFT calculations indicate that the nanorod with more (111) terrace is more stable. The ΔE values are formation energy per atom relative to bulk Au.

Comparison of UPD positions and calculated Pb adsorption energies

The difference in the underpotential shifts for Pb adsorbed at two different sites, ΔV , can be estimated using the difference between the DFT-calculated Pb adsorption energies, ΔE_{ad} as follows:³⁰

$$\Delta V \approx \frac{-\Delta E_{ad}}{2e} \quad (3)$$

$$\Delta E_{ad} = E(\text{slab}+\text{Pb}^*) - E(\text{slab}) - E(\text{Pb}^0) \quad (4)$$

where e is the elementary charge and the factor of 2 comes from the fact that Pb loses two electrons when it dissolves, and $E(\text{Pb}^0)$ refers to the energy of bulk Pb. For Pb adsorption energies, more negative values indicate stronger adsorption. For simplicity, here we assume fairly dilute Pb concentrations, where each Pb atom has no Pb nearest neighbors on the surface; accounting for interactions between adsorbed Pb would result in a more accurate estimate. We present the calculated Pb adsorption energies and corresponding UPD potentials, relative to that of the (111) surface, in Table S3. Pb adsorption energies on (111) facets and other sites on close-packed terraces are similar (Figure S10). We assign these to the left peak, in accordance with experimental results on single crystals.³¹ Pb adsorption energies are higher on other Pb adsorption sites having coordination number of 4 or 5, and these are assigned to the right peak (Table S3).

To estimate the fraction of sites corresponding to each peak, thermodynamically averaged percentages of each type of sites on the 4H and fcc nanorods were recorded during the Monte Carlo simulations (see Methods) and are provided in Table S4. The percentages of Pb sites on the 4H nanoribbons were calculated based on a model surface of 4H(11 $\bar{2}$ 0) with a width of 20 nm and a

thickness of 2.5 nm.³² The sidewall structure of the 4H nanoribbon is the 4H($\bar{1}\bar{1}00$) surface. The results are also provided in Table S4.

There is a correlation between the calculated adsorption energy and Pb coordination number (Figure S10). The 4H($\bar{1}\bar{1}00$) “valley” site in Table S3, which accounts for about ¼ of the 4H surface sites, has a coordination number of 4 and an intermediate adsorption energy. This suggests that the peak and shoulder on the right side of the 4H nanorod Pb_{upd} voltammetric profile (Figure 3a) may correspond to adsorption sites with coordination numbers of 4 and 5, respectively.

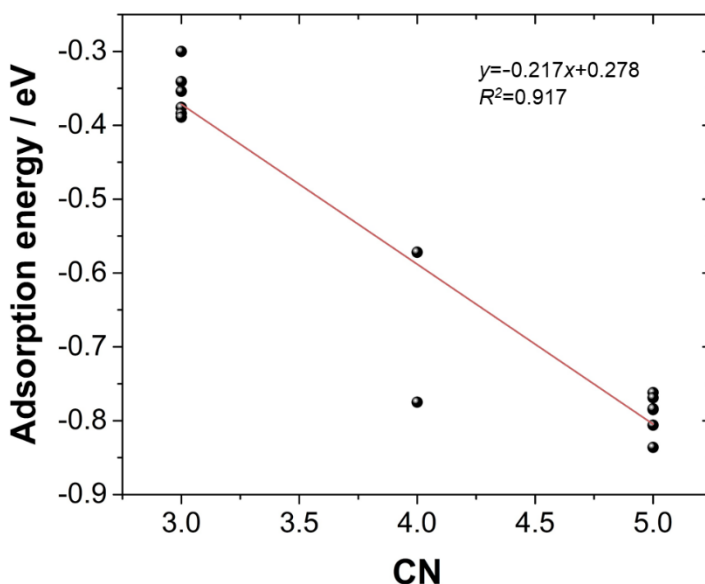
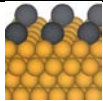

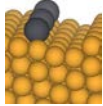
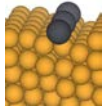
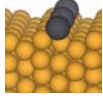
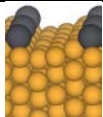
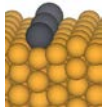

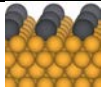
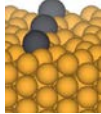
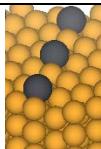
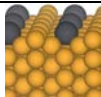
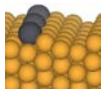
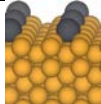


Figure S10. Correlation between the Pb adsorption energy and the coordination number (CN).

Table S3. DFT-calculated Pb adsorption energies at various sites on different Au facets at dilute concentrations, converted to peak positions relative to that of fcc(111) by considering the equation $Pb^{2+} + 2e^- \rightarrow Pb^*$, coordination number (CN) and generalized coordination number (GCN)³³⁻³⁷ of the Pb site. Black and gold spheres represent Pb and Au atoms, respectively.

	CN _{Pb} (GCN)	Adsorption energy / eV	Peak relative to (111) / V	Fraction of sites	Peak position	
(111)	3 (2.500)	-0.300	0	0.68 with (322) and (211) terraces ^a	Left	
(322) terrace	3 (2.333)	-0.341	0.021	0.02	Left	
(322) terrace	3 (2.500)	-0.354	0.027	0.68 with (111) ^a	Left	
(322) terrace	3 (2.500)	-0.376	0.038		Left	
(211) terrace	3 (2.500)	-0.384	0.042		Left	
4H(11̄00) terrace	3 (2.417)	-0.389	0.045	0.16 (ribbon) 0.42 (rod)	Left	
4H(11̄00) valley	4 (3.500)	-0.572	0.136	0.08 (ribbon) 0.24 (rod)	Right	
(322) valley	5 (4.000)	-0.762	0.231	0.12 with (211) valley ^b	Right	

(100)	4 (3.000)	-0.775	0.238	0.16	Right	
4H(11 $\bar{2}$ 0)	5 (3.667)	-0.769	0.235	0.76 (ribbon) ^c	Right	
4H(11 $\bar{2}$ 0)	5 (3.667)	-0.785	0.243	0.34 (rod) ^c	Right	
(110)-rec	5 (4.333)	-0.784	0.242	0.02	Right	
(211) valley	5 (4.000)	-0.806	0.253	0.12 with (322) valley ^b	Right	
(110)	5 (3.667)	-0.836	0.268	0.00	Right	

^a Adsorption sites were classified by their coordination number and generalized coordination number, which is the same for each of these sites.

^b Adsorption sites were classified by their coordination number and generalized coordination number, which is the same for these two sites.

^c Adsorption sites were classified by their coordination number and generalized coordination number which is the same for these two sites.

Table S4. Fraction of surface Pb sites that assigned to left / right UPD peak on the fcc-Au nanorod, 4H-Au nanorod, and 4H-Au nanoribbon.

	fcc-Au nanorod	4H-Au nanorod	4H-Au nanoribbon
Left peak (CN=3)	0.70	0.42	0.16
Right peak (CN=4)	0.16	0.24	0.08
Right peak (CN=5)	0.14	0.34	0.76

Free energy of adsorbates

The free energy change of the CO₂ reduction intermediates at zero potential can be written as:

$$\Delta G = \Delta E_{DFT} + \Delta ZPE - T\Delta S + \Delta \int_{T'=0}^T C_p dT' \quad (5)$$

where ΔE_{DFT} is the electronic energy for the intermediate step of the CO₂ reduction from DFT calculations, ΔZPE is the difference in zero-point energies for a certain reaction, ΔC_p is the difference in constant-pressure heat capacity, ΔS is the change in entropy. At an applied potential U , the change in free energy is shifted by $-neU$ according to the computational hydrogen electrode (CHE):³⁸

$$\Delta G(U) = \Delta E_{DFT} + \Delta ZPE - T\Delta S + \Delta \int_{T'=0}^T C_p dT' - neU \quad (6)$$

where n is the number of ($H^+ + e^-$) transferred. All electronic energies are referenced to the corresponding Au clean slab, graphene (C), H₂ and H₂O. For example, the adsorption energy of CO can be calculated as:

$$\Delta E_{DFT}(*CO) = E_{DFT}(\text{slab}*CO) - E_{DFT}(\text{slab}*) - E(C) - (E(H_2O) - E(H_2)) \quad (7)$$

Table S5. The zero-point energy (ZPE) corrections, entropy (TS) corrections, and enthalpic temperature corrections for adsorbates and non-adsorbates. The values are taken from the work of Peterson *et al.* with T=291.65K.³⁹ We have also applied a +0.32 eV for the free energy of CO₂(g) by Cao *et al.*,²² due to the errors in DFT-calculated reaction enthalpies compared to experimentally measured reaction enthalpies. This value is consistent with the work of Peterson *et al.*³⁹

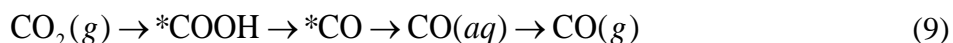
	ZPE / eV	TS / eV	$\int C_p dT$ / eV
*CO	0.192	0.153	0.076
*COOH	0.624	0.178	0.096
*H	0.160	0.007	0.005
CO	0.14	0.60	0.09
CO ₂	0.31	0.65	0.10
H ₂	0.27	0.39	0.09
H ₂ O	0.58	0.65	0.10
C	0.13	0.02	0.026

Free energy diagram and activity

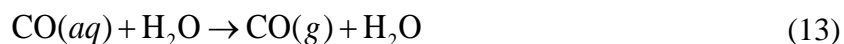
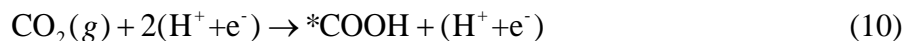
Based on the computational work in the literature, the reaction pathway for CO₂ reduction to CO(g) is likely to be:³⁹⁻⁴¹



We have assumed that the proton and electron transfers are simultaneous,^{39, 42} and our calculations showed that *CO₂⁻ cannot be stabilized in either implicit solvent or explicit solvent. A recent study by Dunwell *et al.* also suggests that the electron transfer (ET) is unlikely to be rate-limiting on Au surfaces.⁴³ Here, we build a two-step kinetic model (also account for *CO desorption in aqueous solution) as follows:



where CO(aq) indicates a single CO molecule desorbed from the Au surfaces in aqueous solution, as described in the work by Cao *et al.*²² We write out the four intermediate reaction steps as:



There exists a roughly linear relationship^{22, 40, 44} between G(*COOH) and G(*CO) on various facets that have been investigated (Figure S11). Using this linear relationship, we can simplify the activation energies for equations (10-13) as a function of the CO binding free energy G(*CO), and

add in the kinetic barrier for the first step $\Delta G_a(*\text{COOH}) = \Delta G(*\text{COOH}) + 0.18 \text{ eV}$ based on the previous work on copper surfaces.⁴⁵

$$\Delta G_1(U) = G_a(*\text{COOH}) - G(\text{CO}_2) + eU = 0.448\Delta G(*\text{CO}) + 0.472 + eU \quad (14)$$

$$\Delta G_2(U) = G(*\text{CO}) - G_a(*\text{COOH}) + eU = 0.552\Delta G(*\text{CO}) - 0.472 + eU \quad (15)$$

$$\Delta G_3(U) = G(\text{CO}(aq)) - G(*\text{CO}) = 0.574 - \Delta G(*\text{CO}) \quad (16)$$

$$\Delta G_4(U) = G(\text{CO}(g)) - G(\text{CO}(aq)) = 0.119 - 0.574 = -0.455 \quad (17)$$

Therefore, we can define an “activity” as the negative of the activation barriers:

$$\begin{aligned} \text{Activity} &= -\max(\Delta G_1(U), \Delta G_2(U), \Delta G_3(U), \Delta G_4(U), 0) \\ &= -\max(0.448\Delta G(*\text{CO}) + 0.472 + eU, 0.574 - \Delta G(*\text{CO}), 0) \end{aligned} \quad (18)$$

In our experiments the partial pressure of CO is typically low (lower than $\sim 1000 \text{ Pa}$), which results in a lower free energy for $\text{CO}(g)$ than $*\text{CO}$ and facilitates CO desorption, validating the assumption of dilute $*\text{CO}$ coverage in our calculations.

To better understand the selectivity of the synthesized catalysts we have also used computational modeling to evaluate the competing reaction, the hydrogen evolution reaction (HER). The rate limiting step for the HER on Au, which binds hydrogen relatively weakly, is believed to be the Volmer step, in which a single hydrogen atom adsorbs on the surface. We calculated the activation free energy for the hydrogen evolution reaction as $\Delta G_a = \Delta G(*\text{H}) + 0.333 \text{ eV}$, where $\Delta G(*\text{H})$ is our calculated adsorption free energy and 0.333 eV maps our calculated free energy of adsorption (0.447 eV on Au(111)) to the rate-limiting activation energy on Au(111) (0.78 eV) calculated by Lindgren *et al.* at 0 V vs the RHE.⁴⁶ For comparison with the CO_2 reduction reaction (CRR), we define a measure of HER activity as follows:

$$\text{Activity} = -\max(\Delta G(*\text{H}) + 0.333 + eU, -\Delta G(*\text{H}), 0) \quad (19)$$

The relative selectivity for the CRR can be estimated by the limiting potential difference between the CRR and the HER.⁴⁷ Specifically,

$$U_L(\text{CRR}) - U_L(\text{HER}) = \frac{1}{e}(-\max(\Delta G(*\text{COOH}) + 0.18 + eU, 0.574 - \Delta G(*\text{CO}), 0) + \max(\Delta G(*\text{H}) + 0.333 + eU, 0)) \quad (20)$$

This can be simplified using the linear fits in Figure S12a-c to provide general trend with respect to coordination number (Figure S13). We have also plotted this difference for individual sites in the same figure. Consistent with the work by Back *et al.*,⁴⁷ we find that the relative selectivity for the CRR decreases with coordination number at small overpotentials (Figure S13a). This is due to the weaker coordination-dependence of $\Delta G(*\text{H})$ compared to that of $\Delta G(*\text{CO})$ and $\Delta G(*\text{COOH})$ (Figure S12). On the top right region of Figure S13c, we find that 4H(11 $\bar{0}$ 0), particularly abundant on the 4H nanorod, is both active and selective for the CRR. Some fcc sites are predicted to be similarly active and no less selective than the sites on the 4H(11 $\bar{2}$ 0) facet, but these sites are predicted to be far less abundant on the fcc nanorods than the (11 $\bar{2}$ 0) sites are on the 4H nanorods (Table S6).

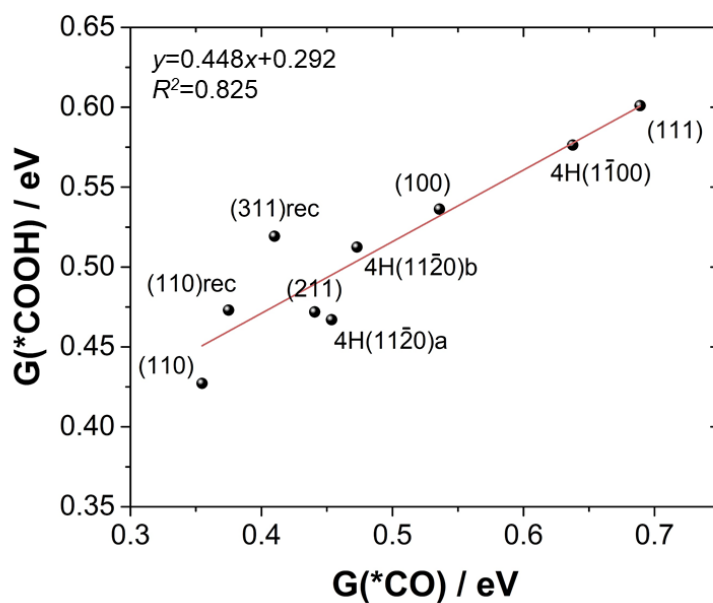


Figure S11. The linear relationship between $G(*COOH)$ and $G(*CO)$. “4H(11 $\bar{2}$ 0) a” and “4H(11 $\bar{2}$ 0) b” represent ridge site “a” and ridge site “b” on this 4H facet, respectively. “4H(1 $\bar{1}$ 00)” represents the ridge site on this 4H facet. “(110)”, “(110)rec”, “(211)”, and “(311)rec” indicate the edge sites on these facets. These are the sites on each facet on which $G(*CO)$ is lowest.

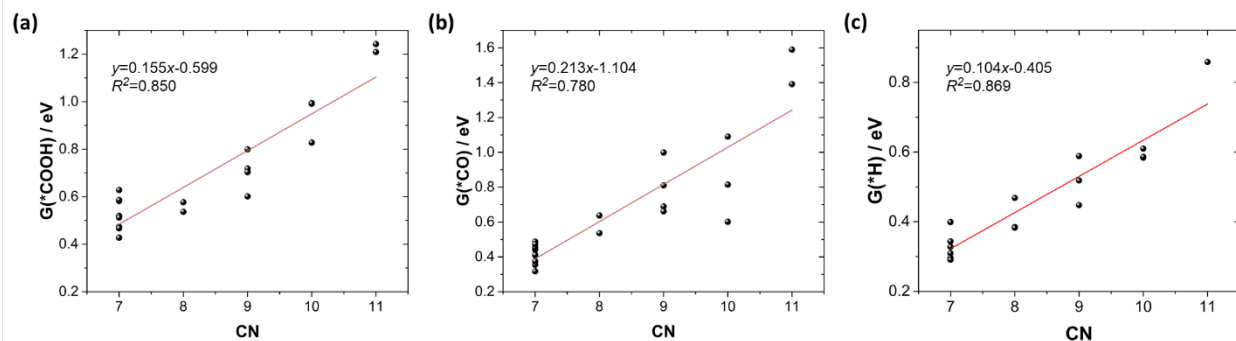


Figure S12. Least-squares fits of $\Delta G(^*\text{COOH})$, $\Delta G(^*\text{CO})$, and $\Delta G(^*\text{H})$ as a function of coordination number (CN).

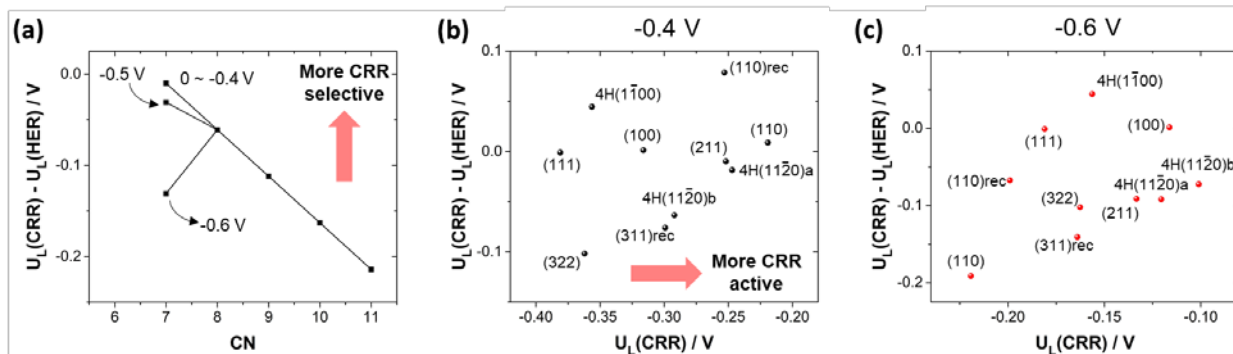


Figure S13. (a) Limiting potential difference $U_L(\text{CRR}) - U_L(\text{HER})$ as a function of coordination number (CN). (b-c) Limiting potential difference as a function of $U_L(\text{CRR})$ at -0.4 V and -0.6 V, respectively. Sites in the top right region are predicted to be more active and relatively more selective for the CO_2 reduction reaction (CRR). “4H(11 $\bar{2}$ 0) a” and “4H(11 $\bar{2}$ 0) b” represent ridge site “a” and ridge site “b” on this 4H facet, respectively. “4H(1 $\bar{1}$ 00)” represents the ridge site on this 4H facet. “(110)”, “(110)rec”, “(211)”, and “(311)rec” indicate the edge sites on these facets. These are the sites on each facet on which $G(^*\text{CO})$ is lowest.

To calculate the average activity for the Au nanostructures, we have explored all possible surface sites on the structures of the fcc and 4H phases taken from room-temperature Monte Carlo simulations. We use the following equation to determine the current at each surface site:

$$j \propto \exp(-\max(\Delta G(*\text{COOH}) + 0.18 + eU, 0.574 - \Delta G(*\text{CO}), 0) / k_B T) \quad (21)$$

where $\Delta G(*\text{COOH})$ and $\Delta G(*\text{CO})$ are adsorption energies of a specific site, and U is the applied potential (see Equations 14-18). For commonly occurring sites, we used DFT to calculate free energies of $*\text{COOH}$ / $*\text{CO}$ adsorption. These free energies, as well as the coordination number (CN) and generalized coordination number (GCN)³³⁻³⁷ of each site, are provided in Table S6. For any surface site with CN and GCN matching one in Table S6, we used DFT-calculated adsorption energies to evaluate equation (21). Sometimes two different sites on the nanorods have the same CN and GCN, e.g. the fcc (211) and (322) step edges, two types of reconstructed (110) edges, and two types of 4H(11 $\bar{2}$ 0) ridge sites (same for valley sites). In first two cases we chose the ones with lower surface energy, which is consistent with the Monte Carlo snapshots; For those two symmetrically distinct 4H(11 $\bar{2}$ 0) sites, we assumed their ratio to be 1:1. For the sites that do not match any within Table S6, we estimated the $*\text{COOH}$ / $*\text{CO}$ adsorption free energies using a linear least-squares fit of DFT-calculated free energies against the CN of the adsorption site (Figure S12).

The surface areas of the Au nanostructures are estimated by:

$$A = \sum_i \left(\frac{A_i}{\#site_i} \right) f_{site_i} N_{site} \quad (22)$$

where $A_i / \#site_i$ is the area per site for site (facet) i , f_{site_i} is the fraction of site i , and N_{site} is the total number of surface sites. The fractions of different types of adsorption sites on the nanorods

were estimated by counting the number of sites matching both the coordination number and generalized coordination number (Table S6). Summing up over the current contributed by all the surface sites and dividing by the surface area yields the specific activity for the nanorods. We plot the activities relative to that of fcc nanorod at -0.3 V (Figure S14). We predict that the activity follows the trend of 4H-Au nanoribbon > 4H-Au nanorod > fcc-Au nanorod; The enhancement of the CO₂RR activity for the 4H nanoribbon is about 3.3 and 23.7 times of that of 4H nanorod and fcc nanorod respectively (at -0.6 V), which is consistent with experiments. Heat maps illustrating the most active sites on the Au nanostructures are shown in Figure S16.

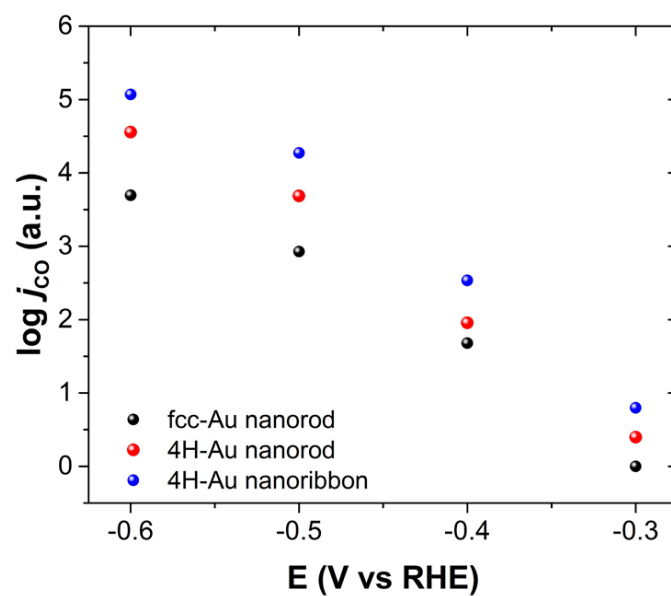
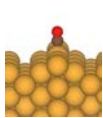

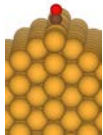
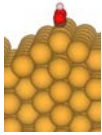
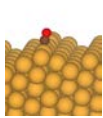
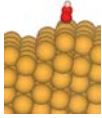
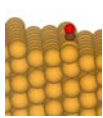
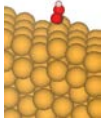

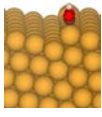
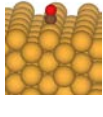
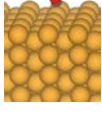

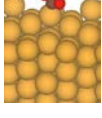
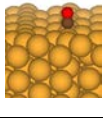
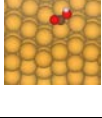
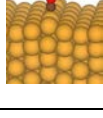
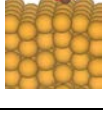
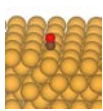
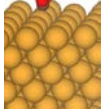
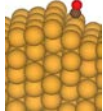
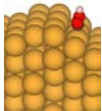
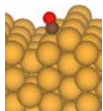
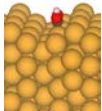
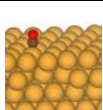
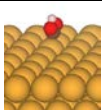
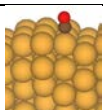
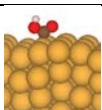
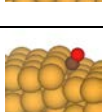
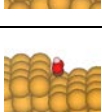
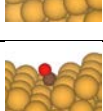
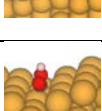
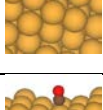
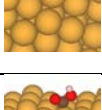
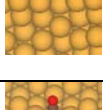
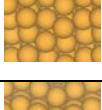
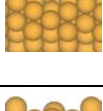
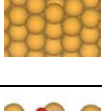


Figure S14. Predicted CO specific activity as a function of potential for the fcc-Au nanorod, 4H-Au nanorod and 4H-Au nanoribbon, relative to that of fcc-Au nanorod at -0.3 V.

Table S6. Generalized coordination number (GCN) and coordination number (CN) of Au, free energy of adsorption of *CO, *COOH, and *H, and fraction of sites on the 4H and fcc nanocrystals for all surface sites studied. Energies are relative to G(CO₂(g)). The suffix “-rec” indicates a reconstructed surface with a missing row, and “-rec2” indicates a reconstructed surface with two missing rows.

	GCN (CN _{Au})	G(*CO) / eV	G(*COOH) / eV	G(*H) / eV	Fraction	*CO	*COOH
(110)-rec edge	5.167 (7)	0.375	0.473	0.295	/		
(110)-rec2 edge (111)/(111)	5.167 (7)	0.317	0.586	0.399			
(311)-rec edge (111)/(100)	5.333 (7)	0.410	0.519	0.291	0.03		
(211) step edge	5.500 (7)	0.441	0.472	0.309	/		
(322) step edge	5.500 (7)	0.411	0.582	0.328			
(110)	5.833 (7)	0.355	0.427	0.399	0.00		
4H(11 $\bar{2}$ 0) ridge “a”	5.833 (7)	0.454	0.467	0.296	0.01 (rod) 0.21 (ribbon)		
4H(11 $\bar{2}$ 0) ridge “b”	5.833 (7)	0.473	0.512	0.296	0.01 (rod) 0.21 (ribbon)		
4H(11 $\bar{1}$ 00) ridge	6.333 (8)	0.638	0.576	0.468	0.12 (rod) 0.04 (ribbon)		

(100)	6.667 (8)	0.535	0.536	0.385	0.02		
(211)-rec terrace (100) micro facet	6.750 (8)	0.661	0.674	0.383	0.02		
(110)-rec terrace	7.167 (9)	0.999	0.799	0.589	0.08		
(111) terrace	7.500 (9)	0.689	0.601	0.447	0.35		
4H(1100) terrace	7.500 (9)	0.811	0.703	0.518	0.14 (rod) 0.09 (ribbon)		
(211) valley	8.750 (10)	0.601	0.993	0.584	0.01		
(311)-rec valley	8.833 (10)	0.815	0.991	0.586	0.01		
4H(1100) valley	8.667 (10)	1.091	0.828	0.610	0.09 (rod) 0.04 (ribbon)		
4H(1120) valley “a”	9.167 (11)	1.391	1.242	0.858	0.01 (rod) 0.21 (ribbon)		
4H(1120) valley “b”	9.167 (11)	1.589	1.209	0.858	0.01 (rod) 0.21 (ribbon)		

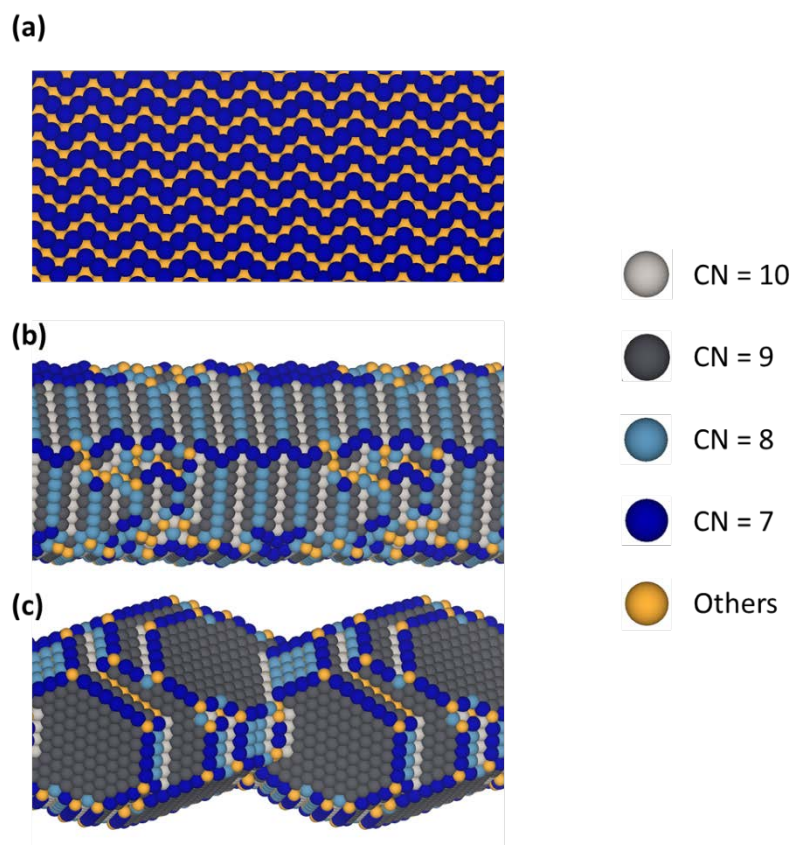


Figure S15. Distribution of surface site coordination numbers of (a) 4H-Au nanoribbon, (b) 4H-Au nanorod and (c) fcc-Au nanorod.

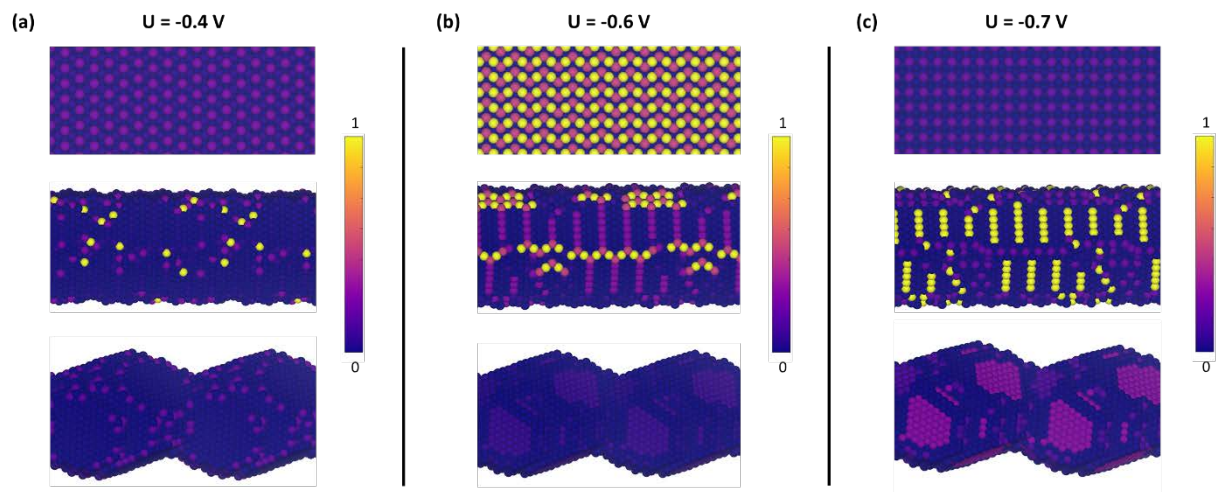


Figure S16. Predicted current density of all surface sites on 4H-Au nanoribbon, 4H-Au nanorod and fcc-Au nanorod, relative to the most active sites at (a) -0.4 V, (b) -0.6 V, and (c) -0.7 V.

References

1. Fan, Z.; Huang, X.; Chen, Y.; Huang, W.; Zhang, H., Facile synthesis of gold nanomaterials with unusual crystal structures. *Nat. Protoc.* **2017**, *12*, 2367.
2. Chen, Y.; Fan, Z.; Luo, Z.; Liu, X.; Lai, Z.; Li, B.; Zong, Y.; Gu, L.; Zhang, H., High-Yield Synthesis of Crystal-Phase-Heterostructured 4H/fcc Au@Pd Core–Shell Nanorods for Electrocatalytic Ethanol Oxidation. *Adv. Mater.* **2017**, *29*, 1701331.
3. Mariano, R. G.; McKelvey, K.; White, H. S.; Kanan, M. W., Selective increase in CO₂ electroreduction activity at grain-boundary surface terminations. *Science* **2017**, *358*, 1187.
4. Sanchez, J. M.; Ducastelle, F.; Gratias, D., Generalized cluster description of multicomponent systems. *Physica A* **1984**, *128*, 334-350.
5. Ising, E., Beitrag zur Theorie des Ferromagnetismus. *Z. Phys.* **1925**, *31*, 253-258.
6. Kohn, W.; Sham, L. J., Self-Consistent Equations Including Exchange and Correlation Effects. *Phys. Rev.* **1965**, *140*, A1133-A1138.
7. Mueller, T.; Ceder, G., Bayesian approach to cluster expansions. *Phys. Rev. B* **2009**, *80*, 024103.
8. Mueller, T., Ab initio determination of structure-property relationships in alloy nanoparticles. *Phys. Rev. B* **2012**, *86*, 144201.
9. Cao, L.; Li, C.; Mueller, T., The Use of Cluster Expansions To Predict the Structures and Properties of Surfaces and Nanostructured Materials. *J. Chem. Inf. Model.* **2018**, *58*, 2401-2413.
10. van de Walle, A.; Ceder, G., Automating first-principles phase diagram calculations. *J. Phase Equilibria Diffus.* **2002**, *23*, 348.
11. Kresse, G.; Furthmüller, J., Efficient iterative schemes for ab initio total-energy calculations using a plane-wave basis set. *Phys. Rev. B* **1996**, *54*, 11169-11186.
12. Perdew, J. P.; Burke, K.; Ernzerhof, M., Generalized Gradient Approximation Made Simple. *Phys. Rev. Lett.* **1996**, *77*, 3865-3868.
13. Hammer, B.; Hansen, L. B.; Nørskov, J. K., Improved adsorption energetics within density-functional theory using revised Perdew-Burke-Ernzerhof functionals. *Phys. Rev. B* **1999**, *59*, 7413-7421.
14. Perdew, J. P.; Ruzsinszky, A.; Csonka, G. I.; Vydrov, O. A.; Scuseria, G. E.; Constantin, L. A.; Zhou, X.; Burke, K., Restoring the Density-Gradient Expansion for Exchange in Solids and Surfaces. *Phys. Rev. Lett.* **2008**, *100*, 136406.
15. Grimme, S.; Antony, J.; Ehrlich, S.; Krieg, H., A consistent and accurate ab initio parametrization of density functional dispersion correction (DFT-D) for the 94 elements H-Pu. *J. Chem. Phys.* **2010**, *132*, 154104.
16. Mathew, K.; Sundararaman, R.; Letchworth-Weaver, K.; Arias, T. A.; Hennig, R. G., Implicit solvation model for density-functional study of nanocrystal surfaces and reaction pathways. *J. Chem. Phys.* **2014**, *140*, 084106.
17. Blöchl, P. E., Projector augmented-wave method. *Phys. Rev. B* **1994**, *50*, 17953-17979.
18. Wisesa, P.; McGill, K. A.; Mueller, T., Efficient generation of generalized Monkhorst-Pack grids through the use of informatics. *Phys. Rev. B* **2016**, *93*, 155109.
19. Methfessel, M.; Paxton, A. T., High-precision sampling for Brillouin-zone integration in metals. *Phys. Rev. B* **1989**, *40*, 3616-3621.
20. Fishman, M.; Zhuang, H. L.; Mathew, K.; Dirschka, W.; Hennig, R. G., Accuracy of exchange-correlation functionals and effect of solvation on the surface energy of copper. *Phys. Rev. B* **2013**, *87*, 245402.
21. Kim, J.; Samano, E.; Koel, B. E., CO Adsorption and Reaction on Clean and Oxygen-Covered Au(211) Surfaces. *J. Phys. Chem. B* **2006**, *110*, 17512-17517.
22. Cao, L.; Raciti, D.; Li, C.; Livi, K. J. T.; Rottmann, P. F.; Hemker, K. J.; Mueller, T.; Wang, C., Mechanistic Insights for Low-Overpotential Electroreduction of CO₂ to CO on Copper Nanowires. *ACS Catal.* **2017**, *7*, 8578-8587.
23. Metropolis, N.; Rosenbluth, A. W.; Rosenbluth, M. N.; Teller, A. H.; Teller, E., Equation of State Calculations by Fast Computing Machines. *J. Chem. Phys.* **1953**, *21*, 1087-1092.

24. Zhu, W.; Michalsky, R.; Metin, Ö.; Lv, H.; Guo, S.; Wright, C. J.; Sun, X.; Peterson, A. A.; Sun, S., Monodisperse Au Nanoparticles for Selective Electrocatalytic Reduction of CO₂ to CO. *J. Am. Chem. Soc.* **2013**, *135*, 16833-16836.
25. Kim, D.; Resasco, J.; Yu, Y.; Asiri, A. M.; Yang, P., Synergistic geometric and electronic effects for electrochemical reduction of carbon dioxide using gold–copper bimetallic nanoparticles. *Nat. Commun.* **2014**, *5*, 4948.
26. Lee, H.-E.; Yang, K. D.; Yoon, S. M.; Ahn, H.-Y.; Lee, Y. Y.; Chang, H.; Jeong, D. H.; Lee, Y.-S.; Kim, M. Y.; Nam, K. T., Concave Rhombic Dodecahedral Au Nanocatalyst with Multiple High-Index Facets for CO₂ Reduction. *ACS Nano* **2015**, *9*, 8384-8393.
27. Feng, X.; Jiang, K.; Fan, S.; Kanan, M. W., Grain-Boundary-Dependent CO₂ Electroreduction Activity. *J. Am. Chem. Soc.* **2015**, *137*, 4606-4609.
28. Kim, C.; Jeon, H. S.; Eom, T.; Jee, M. S.; Kim, H.; Friend, C. M.; Min, B. K.; Hwang, Y. J., Achieving Selective and Efficient Electrocatalytic Activity for CO₂ Reduction Using Immobilized Silver Nanoparticles. *J. Am. Chem. Soc.* **2015**, *137*, 13844-13850.
29. Yoon, Y.; Hall, A. S.; Surendranath, Y., Tuning of Silver Catalyst Mesostructure Promotes Selective Carbon Dioxide Conversion into Fuels. *Angew. Chem. Inter. Ed. Engl.* **2016**, *55*, 15282-15286.
30. Leiva, E., Recent developments in the theory of metal upd. *Electrochim. Acta* **1996**, *41*, 2185-2206.
31. Hernández, J.; Solla-Gullón, J.; Herrero, E., Gold nanoparticles synthesized in a water-in-oil microemulsion: electrochemical characterization and effect of the surface structure on the oxygen reduction reaction. *J. Electroanal. Chem.* **2004**, *574*, 185-196.
32. Fan, Z.; Bosman, M.; Huang, X.; Huang, D.; Yu, Y.; Ong, K. P.; Akimov, Y. A.; Wu, L.; Li, B.; Wu, J.; Huang, Y.; Liu, Q.; Eng Png, C.; Lip Gan, C.; Yang, P.; Zhang, H., Stabilization of 4H hexagonal phase in gold nanoribbons. *Nat. Commun.* **2015**, *6*, 7684.
33. Federico, C. V.; I., M. J.; M., G. L. J.; Philippe, S.; David, L., Fast Prediction of Adsorption Properties for Platinum Nanocatalysts with Generalized Coordination Numbers. *Angew. Chem. Inter. Ed. Engl.* **2014**, *53*, 8316-8319.
34. Calle-Vallejo, F.; Tymoczko, J.; Colic, V.; Vu, Q. H.; Pohl, M. D.; Morgenstern, K.; Loffreda, D.; Sautet, P.; Schuhmann, W.; Bandarenka, A. S., Finding optimal surface sites on heterogeneous catalysts by counting nearest neighbors. *Science* **2015**, *350*, 185-189.
35. Li, H.; Li, Y.; Koper, M. T. M.; Calle-Vallejo, F., Bond-Making and Breaking between Carbon, Nitrogen, and Oxygen in Electrocatalysis. *J. Am. Chem. Soc.* **2014**, *136*, 15694-15701.
36. Calle-Vallejo, F.; Koper, M. T. M.; Bandarenka, A. S., Tailoring the catalytic activity of electrodes with monolayer amounts of foreign metals. *Chem. Soc. Rev.* **2013**, *42*, 5210-5230.
37. Kleis, J.; Greeley, J.; Romero, N. A.; Morozov, V. A.; Falsig, H.; Larsen, A. H.; Lu, J.; Mortensen, J. J.; Dułak, M.; Thygesen, K. S.; Nørskov, J. K.; Jacobsen, K. W., Finite Size Effects in Chemical Bonding: From Small Clusters to Solids. *Catal. Lett.* **2011**, *141*, 1067-1071.
38. Nørskov, J. K.; Rossmeisl, J.; Logadottir, A.; Lindqvist, L.; Kitchin, J. R.; Bligaard, T.; Jónsson, H., Origin of the Overpotential for Oxygen Reduction at a Fuel-Cell Cathode. *J. Phys. Chem. B* **2004**, *108*, 17886-17892.
39. Peterson, A. A.; Abild-Pedersen, F.; Studt, F.; Rossmeisl, J.; Nørskov, J. K., How copper catalyzes the electroreduction of carbon dioxide into hydrocarbon fuels. *Energy Environ. Sci.* **2010**, *3*, 1311-1315.
40. Cheng, T.; Huang, Y.; Xiao, H.; Goddard, W. A., Predicted Structures of the Active Sites Responsible for the Improved Reduction of Carbon Dioxide by Gold Nanoparticles. *J. Phys. Chem. Lett.* **2017**, *8*, 3317-3320.
41. Hansen, H. A.; Varley, J. B.; Peterson, A. A.; Nørskov, J. K., Understanding Trends in the Electrocatalytic Activity of Metals and Enzymes for CO₂ Reduction to CO. *J. Phys. Chem. Lett.* **2013**, *4*, 388-392.

42. Durand, W. J.; Peterson, A. A.; Studt, F.; Abild-Pedersen, F.; Nørskov, J. K., Structure effects on the energetics of the electrochemical reduction of CO₂ by copper surfaces. *Surf. Sci.* **2011**, *605*, 1354-1359.
43. Dunwell, M.; Luc, W.; Yan, Y.; Jiao, F.; Xu, B., Understanding Surface-Mediated Electrochemical Reactions: CO₂ Reduction and Beyond. *ACS Catal.* **2018**, 8121-8129.
44. Liu, X.; Xiao, J.; Peng, H.; Hong, X.; Chan, K.; Nørskov, J. K., Understanding trends in electrochemical carbon dioxide reduction rates. *Nat. Commun.* **2017**, *8*, 15438.
45. Shi, C.; Chan, K.; Yoo, J. S.; Nørskov, J. K., Barriers of Electrochemical CO₂ Reduction on Transition Metals. *Org. Process Res. Dev.* **2016**, *20*, 1424-1430.
46. Lindgren, P.; Kastlunger, G.; Peterson, A. A., A challenge to the Delta G⁰ interpretation of hydrogen evolution. *ACS Catal.* **2019**, *10*, 121-128.
47. Back, S.; Yeom, M. S.; Jung, Y., Understanding the Effects of Au Morphology on CO₂ Electrocatalysis. *J. Phys. Chem. C* **2018**, *122*, 4274-4280.